

Possible scenario of dynamical chiral symmetry breaking in the interacting instanton liquid model

Yamato Suda¹ and Daisuke Jido¹

¹*Department of Physics, Tokyo Institute of Technology,
2-12-1 Ookayama, Meguro, Tokyo 152-8551, Japan*

(Dated: February 9, 2024)

We compute the vacuum energy density as a function of the quark condensate in the interacting instanton liquid model (IILM) and examine the pattern of dynamical chiral symmetry breaking from its behavior around the origin. This evaluation is performed by using simulation results of the IILM. We find that chiral symmetry is broken in the $U(1)_A$ anomaly assisted way in the IILM with three-flavor dynamical quarks. We call such a symmetry breaking the anomaly-driven breaking which is one of the scenarios of chiral symmetry breaking proposed in the context of the chiral effective theories. We also find that the instanton-quark interaction included in the IILM plays a crucial role for the anomaly-driven breaking by comparing the full and the quenched IILM calculations.

I. INTRODUCTION

In hadron physics, chiral symmetry and its dynamical breaking have led to our systematic understanding of hadron spectra. For instance, the arrangement of light pseudoscalar (π, K, \bar{K}, η)-mesons can be explained through the dynamical breaking of $SU(3)_L \times SU(3)_R$ flavor symmetry as the Nambu-Goldstone theorem states. On the other hand, mesons like $f_0(500)$ are still puzzles in hadron physics [1, 2]. The characteristics of $f_0(500)$, such as its existence, mass and internal structure, have been under discussion for a long time [3–21]. The σ meson that is recognized as the chiral partner of the pion is one of the candidates of $f_0(500)$ because it should exist in the state $J^P = 0^+$ if chiral symmetry is manifested in the low-energy regime of quantum chromodynamics (QCD). Since the σ meson emerges as a fluctuation of an order parameter of chiral symmetry, there is a growing need to systematically investigate the chiral dynamics.

In revealing such hadron properties, we need to understand the pattern of dynamical chiral symmetry breaking of QCD. Many models have been proposed to describe the dynamical chiral symmetry breaking [22–24]. A notable example is the Nambu-Jona-Lasinio (NJL) model which exhibits essential features of QCD and provides a mathematically traceable framework under the mean field approximation. In this model, the attractive interaction among quark fields induces the quark condensate in the vacuum and it breaks chiral symmetry. As chiral symmetry is broken dynamically, pseudoscalar mesons become the massless Nambu-Goldstone bosons, while their chiral partners, the scalar mesons, acquire finite masses. Furthermore, the inclusion of the $U(1)_A$ anomaly enables us to comprehend the spectrum of pseudoscalar mesons including η and η' [25–27]. Comprehensive understanding of the pattern and mechanism of dynamical chiral symmetry breaking is one of the keys to unraveling the properties of hadrons and the QCD vacuum on which they rely.

Recently, the chiral effective theories have shown that the different patterns of dynamical chiral symmetry

breaking predict the different values of the σ mass [28]. In the NJL model without the $U(1)_A$ anomaly term, chiral symmetry breaks dynamically when the interquark attractive interaction is sufficiently strong. With the presence of the $U(1)_A$ anomaly term, chiral symmetry is broken dynamically even if the four-point interquark interaction is smaller than its critical value as long as the contribution from the $U(1)_A$ anomaly is significant (which we call anomaly-driven symmetry breaking). The mass of the σ meson assumed as the chiral partner of the pion shows that in the former case it is larger than approximately 800 MeV, while in the latter case it is smaller than about 800 MeV [28]. These findings are derived from analyses using the linear sigma model and the NJL model, while the universality of their consequence remains unclear in other systems.

In this paper, we examine whether the anomaly-driven breaking of chiral symmetry universally realizes in the context of other than the chiral effective models. The realization of the anomaly-driven breaking is identified by the quark condensate dependence of the vacuum energy density. This characteristic is deduced from the discussion within the chiral effective models [28]. We generalize this concept to validate it in other models using the curvature of the vacuum energy density with respect to the quark condensate at the origin. As an example of its application, we use the interacting instanton liquid model (IILM). The IILM is a phenomenological model that describes the chiral symmetry breaking by treating the QCD vacuum as a superposition of instantons [29, 30]. Since the instanton results in the $U(1)_A$ anomaly [31], we discuss the possibility of the anomaly-driven symmetry breaking using the IILM that has both features like the chiral symmetry breaking and the $U(1)_A$ anomaly related to the instantons.

This paper is organized as follows. In Sect. II, we introduce the definition of anomaly-driven breaking of chiral symmetry in the NJL model and other models. In Sect. III, we describe the formulation of the IILM that is used in this study and details the numerical simulations. In Sect. IV, we present the simulation results of the IILM

and discuss their interpretations. In Sect. V, we conclude this paper.

II. ANOMALY-DRIVEN BREAKING OF CHIRAL SYMMETRY

In this section, we introduce the definition of the anomaly-driven chiral symmetry breaking in the NJL model and other models.

A. Anomaly-driven breaking in the NJL model

We briefly explain the anomaly-driven breaking of chiral symmetry which was proposed by the previous work [28] based on the three flavor NJL model with the axial anomaly term. In Ref. [28], the following Lagrangian is considered:

$$\begin{aligned} \mathcal{L}_{\text{NJL}} = & \bar{\psi}(i\gamma^\mu\partial_\mu - \mathcal{M})\psi \\ & + g_S \sum_{a=0}^8 \left[\left(\bar{\psi} \frac{\lambda_a}{2} \psi \right)^2 + \left(\bar{\psi} i\gamma_5 \frac{\lambda_a}{2} \psi \right)^2 \right] \\ & + \frac{g_D}{2} \left\{ \det_{i,j} [\bar{\psi}_i (1 - \gamma_5) \psi_j] + \text{H.c.} \right\}, \end{aligned} \quad (1)$$

for the quark fields $\psi = (u, d, s)^T$, where \mathcal{M} is the quark mass matrix given by $\mathcal{M} = \text{diag}(m_q, m_q, m_s)$ with assuming isospin symmetry $m_q = m_u = m_d$, λ_a ($a = 0, 1, \dots, 8$) represent the Gell-Mann matrices in the flavor space with $\lambda_0 = \sqrt{2/3}\mathbf{1}$, $\det_{i,j}$ is understood as determinant operation over the flavor indices of the quark fields $\psi_i, \bar{\psi}_j$ ($i, j = u, d, s$), and g_S, g_D are the coupling constants for the four-point vertex interaction and the determinant-type $U(1)_A$ breaking interaction, respectively. In the mean field approximation, the effective potential is obtained from the Lagrangian (1) as a function of the dynamical quark mass M as follows

$$\begin{aligned} V_{\text{eff}}(M) = & iN_c \sum_{f=q,q,s} \int \frac{d^4p}{(2\pi)^4} \text{Tr} \left[\ln(\gamma \cdot p - M_f) + \frac{\gamma \cdot p - m_f}{\gamma \cdot p - M_f} \right] \\ & - \frac{g_S}{2} (2\langle \bar{q}q \rangle^2 + \langle \bar{s}s \rangle) - g_D \langle \bar{q}q \rangle^2 \langle \bar{s}s \rangle, \end{aligned} \quad (2)$$

where $\langle \bar{q}q \rangle = \langle \bar{u}u \rangle = \langle \bar{d}d \rangle$ is the quark condensate with isospin symmetry and is given as a function of M . Their specific forms are given by Eq. (A.1) and Eq. (A.2) in Ref. [28].

Following Ref. [28], we start with the case of the chiral limit and no anomaly term, i.e., $m_q = m_s = 0$ and $g_D = 0$ in Eq. (1). In this situation, chiral symmetry is dynamically broken at the vacuum with a finite dynamical quark mass when the dimensionless coupling constant $G_S \equiv g_S/g_S^{\text{crit}}$ is larger than 1. Here, g_S^{crit} is the critical coupling constant defined by $g_S^{\text{crit}} = 2\pi^2/(3\Lambda_3^2)$ with

a three-momentum cutoff Λ_3 for the quark loop function. In other words, if there exists sufficiently strong four-quark interaction, chiral symmetry is dynamically broken in the vacuum. This is the well-known scenario of the dynamical chiral symmetry breaking in the NJL model.

Next, let us take the anomaly term into account with $g_D \neq 0$ in Eq. (1) while keeping the chiral limit. In this situation, even though G_S is less than 1, chiral symmetry can be broken dynamically in the vacuum due to the existence of the axial anomaly term. The previous work [28] demonstrated that such a situation is realized with a sufficiently large contribution from the anomaly term. We refer to such chiral symmetry breaking as the anomaly-driven breaking of chiral symmetry or shortly the anomaly-driven breaking in this paper.

The above patterns of the chiral symmetry breaking are related to the hadronic properties, such as the mass of the σ meson [28]. In the literature, in order to study the relationship more quantitatively, the explicit chiral symmetry breaking by finite current quark mass is introduced and the σ meson is assumed to be the chiral partner of the pion. The authors calculated the σ meson mass with varying values of the dimensionless couplings G_S and $G_D \equiv \Lambda_3 g_D / (g_S^{\text{crit}})^2$ so as to reproduce the η' mass. As a result, they found that the σ mass is smaller than about 800 MeV when the anomaly-driven breaking is realized, i.e., $G_S < 1$, and larger than about 800 MeV if the normal breaking is done, i.e., $G_S > 1$.

According to the previous work [28], the definition of the anomaly-driven breaking in the NJL model is that the chiral symmetry is dynamically broken even though the dimensionless coupling constant G_S is less than 1. However, the definition of this determination procedure relies on the model-specific parameter G_S , which makes its application to other models nontrivial. To discuss the anomaly-driven breaking in other models and systems, in the next section, we generalize the definition of the determination procedure for the anomaly-driven breaking.

B. The anomaly-driven breaking in other models

In this subsection, we generalize the definition of the determination procedure for anomaly-driven breaking based on arguments in the NJL model. The anomaly-driven breaking of chiral symmetry was initially introduced in the chiral effective models using the model-specific coupling constants. Here, we present a key quantity that links the model-specific and the model-independent determination procedures for the anomaly-driven breaking. That is the sign of the curvature of the effective potential at the point with zero quark condensate. We use the latter as the definition of determination procedure for the anomaly-driven breaking in this paper.

We first consider the NJL model with no anomaly term in the vanishing quark mass limit ($m \rightarrow 0$). In this case, as we have mentioned in the last section, chiral symmetry

is dynamically broken in the vacuum when a dimensionless four-quark coupling G_S is greater than 1. Here, the evaluation of the second derivative of the effective potential (2) with respect to the quark condensate at the point $\langle \bar{q}q \rangle = 0$ yields the following result:

$$\left. \frac{\partial^2 V_{\text{eff}}}{\partial \langle \bar{q}q \rangle^2} \right|_{\langle \bar{q}q \rangle=0} = g_S^{\text{crit}} - g_S = g_S^{\text{crit}} (1 - G_S), \quad (3)$$

where we use $G_S = g_S/g_S^{\text{crit}}$. From Eq. (3), we find that the parameter region where chiral symmetry is dynamically broken is linked to the negativity of the curvature of the effective potential at the origin. We refer to such chiral symmetry breaking as the normal breaking in contrast to the anomaly-driven one.

Next, let us turn on the anomaly term by $g_D \neq 0$ while keeping the chiral limit. Again, chiral symmetry can be dynamically broken and that leads to the nonzero quark condensate in the vacuum. The main difference compared to the case without the anomaly term is that chiral symmetry can be broken dynamically even though the dimensionless coupling G_S is less than 1. Calculating the second derivative of the effective potential (2) with the anomaly term, we obtain the same result to Eq. (3). Thus, the pattern of dynamical chiral symmetry breaking which is distinguished whether G_S is greater than 1 or not corresponds directly to the sign of the curvature (3).

In Fig. 1, we show the effective potentials as a function of the absolute value of quark condensate for four parameter sets in the chiral limit. In order to set the origin to zero, irrelevant constants are subtracted from the effective potentials. We can see that when the dimensionless coupling G_S is greater than 1, the curvature of effective potential at the origin is negative (red dotted line). On the other hand, when chiral symmetry is dynamically broken even though G_S is less than 1 (green solid line), the curvature is positive at the origin. For the remaining two parameter sets (magenta dash-dotted and blue dashed line), the effective potential has a minimum value at the origin and thus chiral symmetry is not broken in the vacuum. In this way, when the chiral symmetry is dynamically broken, the dimensionless coupling constant G_S and the curvature of the effective potential at the origin are linked in the NJL model including the anomaly term for the chiral limit.

We also confirm that such a relationship between the dimensionless coupling G_S and the curvature of the effective potential remains unchanged even if small current quark masses are introduced. The current quark mass dependence appears in the effective potential as a product with the linear term of the quark condensate for small quark masses. That term vanishes by performing the second derivative with respect to the quark condensate. Equation (3) thus remains the same in the presence of small current quark masses.

Based on the arguments in the NJL model, we use the curvature of the effective potential to determine whether the anomaly-driven breaking or not, instead of the model

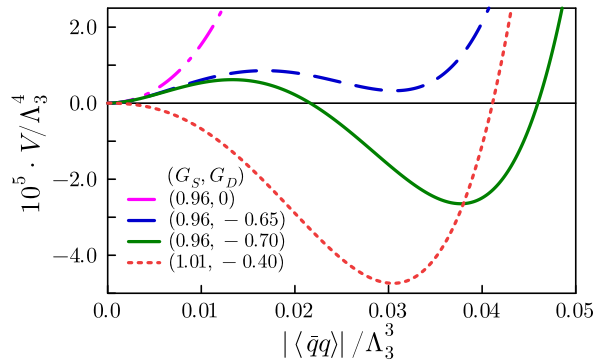


FIG. 1. The effective potentials as a function of the quark condensate normalized by the cutoff scale Λ_3^3 . The mean field approximation is used and the chiral limit is assumed. For the effective potential, the irrelevant constant is subtracted from that. The different coupling constants are plotted, $(G_S, G_D) = (0.96, 0.0)$ [dashed-dotted, magenta]; $(0.96, -0.65)$ [dashed, blue]; $(0.96, -0.70)$ [solid, green]; $(1.01, -0.40)$ [dotted, red].

specific coupling constant. Since the effective potential is proportional to the vacuum energy density ϵ except for a constant in field theory, we take the inequality

$$\left. \frac{\partial^2 \epsilon}{\partial \langle \bar{q}q \rangle^2} \right|_{\langle \bar{q}q \rangle=0} > 0, \quad (4)$$

to be the definition of the determination procedure for the anomaly-driven breaking also for finite quark masses. We apply this definition to the instanton liquid model and discuss the feasibility of the anomaly-driven chiral symmetry breaking.

III. FORMULATION

In the present section, we describe the model and numerical calculation method we used.

A. Interacting instanton liquid model

The QCD Euclid partition function is approximated by the superposition of instantons [33]. The canonical partition function is given as

$$Z = \frac{1}{N_+! N_-!} \int \prod_{i=1}^{N_+ + N_-} [d\Omega_i f(\rho_i)] \exp(-S_{\text{int}}) \times \prod_{f=1}^{N_f} \text{Det}(\not{D} + m_f). \quad (5)$$

Here, N_+ and N_- are the numbers of instantons and anti-instantons, respectively, $d\Omega_i = dU_i d\rho_i d^4 z_i$ is the measure

of the path integral over the collective coordinate space for the color orientation in the color $SU(N_c)$ group, size and position associated with the i -th instanton, and $f(\rho)$ is semiclassical instanton amplitude. The interactions between instanton-instanton and instanton-quark are included in S_{int} and $\text{Det}(\not{D} + m_f)$, respectively. D_μ and m_f represent the covariant derivative for the quark fields and the current quark mass of flavor f , respectively.

The explicit expression of the semiclassical instanton amplitude calculated by 't Hooft [27] reads

$$\begin{aligned} f(\rho) &= C_{N_c} \left[\frac{8\pi^2}{g^2(\rho)} \right]^{2N_c} \exp \left[-\frac{8\pi^2}{g^2(\rho)} \right] \frac{1}{\rho^5} \\ &= C_{N_c} \frac{1}{\rho^5} \beta_1(\rho)^{2N_c} \\ &\quad \times \exp \left[-\beta_2(\rho) + \left(2N_c - \frac{b'}{2b} \right) \frac{b'}{2b} \frac{1}{\beta_1(\rho)} \ln \beta_1(\rho) \right] \\ &\quad + \mathcal{O}(3\text{-loop}), \end{aligned} \quad (6)$$

$$C_{N_c} = \frac{0.466e^{-1.679N_c}}{(N_c - 1)!(N_c - 2)!}, \quad (7)$$

where the gauge coupling g^2 is given as a function of the instanton size ρ , the beta functions β_1, β_2 include up to 2-loop order and the Gell-Mann–Low coefficients are given as follows:

$$\beta_1(\rho) = -b \ln(\rho\Lambda), \quad \beta_2(\rho) = \beta_1(\rho) + \frac{b'}{2b} \ln \left[\frac{2}{b} \beta_1(\rho) \right], \quad (8)$$

$$b = \frac{11}{3}N_c - \frac{2}{3}N_f, \quad b' = \frac{34}{3}N_c^2 - \frac{13}{3}N_cN_f + \frac{N_f}{N_c}. \quad (9)$$

Here, N_c and N_f denote the number of colors and of the dynamical quark flavors, respectively, and Λ is the scale parameter which is introduced for calculating β -function by using the Pauli-Villars regularization scheme [33].

The instanton-instanton interaction S_{int} in Eq. (5) is expressed by the sum of all possible pairs of instantons

$$S_{\text{int}} = \sum_{l < m, l \neq m}^{N_+ + N_-} S_{\text{int}}^{(2)}(l, m), \quad (10)$$

where l, m refer to each instanton or anti-instanton in the ensemble. The two-body interaction between instantons (or anti-instantons) $S_{\text{int}}^{(2)}(l, m)$ is defined as the difference between the action of two-instanton configuration and twice of the single instanton action $S_0(\rho) = 8\pi/g^2(\rho)$:

$$S_{\text{int}}^{(2)}(l, m) = S[A_\mu(l, m)] - 2S_0. \quad (11)$$

Two-instanton configuration is no longer an exact solution to the classical Yang-Mills equations. To calculate the two-body interaction, one uses an *Ansatz* for the gauge configurations. This idea was developed by Schäfer and Shuryak [32, 33]. We use the streamline

Ansatz [34, 35] and its form of S_{int} is given by Eq. (A5) in Ref. [33].

The instanton-quark interaction represented by the determinant in Eq. (5) is evaluated by factorizing it into two parts, a high and a low momentum parts as

$$\text{Det}(\not{D} + m_f) = \text{Det}_{\text{high}}(\not{D} + m_f) \text{Det}_{\text{low}}(\not{D} + m_f). \quad (12)$$

The high momentum part is evaluated as the product of contributions of each instanton calculated by using the Gaussian approximation. The low momentum part is evaluated by using the quark zero-mode wave functions in the instanton and anti-instanton backgrounds [33]. As a result, the instanton-quark interaction takes the following form:

$$\begin{aligned} \text{Det}(\not{D} + m_f) &= \left(\prod_{i=1}^{N_+ + N_-} 1.34\rho_i \right) \text{Det}_{\text{I}, \bar{\text{I}}}(-iT + m_f \mathbf{1}), \\ T &= \begin{pmatrix} \mathbf{0}_{N_+ \times N_+} & (\mathcal{T})_{N_+ \times N_-} \\ (\mathcal{T}^\dagger)_{N_- \times N_+} & \mathbf{0}_{N_- \times N_-} \end{pmatrix}, \end{aligned} \quad (13)$$

$$(\mathcal{T})_{IJ} = \int d^4x \psi_{0,I}^*(x; U, \rho, z) i\gamma_\mu D_\mu \psi_{0,J}(x; U, \rho, z). \quad (14)$$

Here T is called the overlap matrix with a size of $(N_+ + N_-) \times (N_+ + N_-)$. This matrix is spanned by the quark zero-mode wave functions $\psi_{0,I}(x; U, \rho, z)$ in the instanton (I) and anti-instanton ($\bar{\text{I}}$) backgrounds which are labeled by the collective coordinate $\{U, \rho, z\}$. The specific forms of the quark zero-mode wavefunctions are summarized in Appendix 2 of Ref. [32]. The determinant operation $\text{Det}_{\text{I}, \bar{\text{I}}}$ is taken over the space represented in Eq. (13) and $m_f \mathbf{1}$ is understood as a diagonal matrix of $(N_+ + N_-) \times (N_+ + N_-)$. The explicit expression of \mathcal{T} is given by Eq. (B2) in Ref. [33].

In this paper, we work on the $SU(3)$ flavor symmetric limit, i.e., the number of quark flavors is set to $N_f = 3$ and the current quark masses are equally set to $m = m_f$ ($f = 1, 2, 3$). The quark condensate $\langle \bar{q}q \rangle$ represents the one-flavor amount for our calculations.

B. Free energy in instanton ensemble

The vacuum energy density is identified the free energy density as $\epsilon = F$ at zero temperature and we simply call it the free energy denoted as F in what follows. This relationship is derived from the standard thermodynamics relation. The free energy is expressed as

$$F = -\frac{1}{V} \ln Z, \quad (15)$$

with the four-dimensional space-time volume $V = L^4$ and the partition function Z of the system considered.

We explain the method to compute the value of the partition function Z . The method that we use is well-known as the thermodynamics integration method, and it

has been applied to the ILM calculation in the previous work [33]. In this method, one writes the effective action as

$$S_{\text{eff}}(\alpha) = S_{\text{eff}}(0) + \alpha S_1, \quad (16)$$

with the partition function $Z(\alpha) = \int d\Omega \exp[-S_{\text{eff}}(\alpha)]$. The desired partition function Z is reproduced as $Z(\alpha = 1)$. This form of the effective action (16) interpolates between a known solvable action $S_{\text{eff}}(0) \equiv S_{\text{eff}}^0$ and the full action $S_{\text{eff}}(1) = S_{\text{eff}}^0 + S_1$. One obtains the partition function $Z(\alpha = 1)$ straightforwardly as

$$\ln[Z(\alpha = 1)] = \ln[Z(\alpha = 0)] - \int_0^1 d\alpha \langle 0|S_1|0 \rangle_\alpha, \quad (17)$$

where the expectation value $\langle 0|O|0 \rangle_\alpha$ is defined by

$$\langle 0|O|0 \rangle_\alpha \equiv \frac{1}{Z(\alpha)} \int d\Omega O(\Omega) e^{-S_{\text{eff}}(\alpha)}, \quad (18)$$

with configurations according to $p(\Omega_i) \propto \exp[-S_{\text{eff}}(\alpha)]$. Therefore, if we know the decomposition (16) and the values of S_{eff}^0 and $Z(\alpha = 0)$, we can compute the partition function $Z(\alpha = 1)$ from Eq. (17).

For our computation of the partition function in the instanton liquid model, we use the following decomposition of the effective action S_{eff} as Ref. [33]:

$$S_{\text{eff}}(\alpha) = \sum_{i=1}^{N_+ + N_-} \left\{ \ln[f(\rho_i)] + (1 - \alpha) \nu \frac{\rho_i^2}{\bar{\rho}^2} \right\} + \alpha \left[S_{\text{int}} - \sum_{f=1}^{N_f} \ln \text{Det}(\not{D} + m_f) \right], \quad (19)$$

where $\nu = (b - 4)/2$ is a coefficient with the Gell-Mann–Low coefficient b given by Eq. (9), and $\bar{\rho}^2$ is the average size squared of instantons in the full ensembles including the instanton-instanton and instanton-quark interactions. The variational single instanton distribution is used as $Z(\alpha = 0) \equiv Z_0$. Its form is given by

$$Z_0 = \frac{1}{N_+! N_-!} (V \mu_0)^{N_+ + N_-}, \quad (20)$$

with

$$\mu_0 = \int_0^\infty d\rho f(\rho) \exp\left(-\nu \frac{\rho^2}{\bar{\rho}^2}\right). \quad (21)$$

C. Quark condensate in instanton ensemble

In the instanton liquid model, the quark condensate is evaluated as the expectation value of the traced quark

propagator at the same space-time coordinate as follows:

$$\begin{aligned} \langle \bar{q}q \rangle &= \sum_{A, \alpha} \langle q^\dagger(x)_\alpha^A q(x)_\alpha^A \rangle \\ &= - \lim_{y \rightarrow x} \sum_{A, \alpha} \langle q(x)_\alpha^A q^\dagger(y)_\alpha^A \rangle \\ &= - \lim_{y \rightarrow x} \frac{1}{Z} \int D\Omega \text{Tr}[S(x, y; m)] e^{-S_{\text{int}}} \text{Det}(\not{D} + m). \end{aligned} \quad (22)$$

Here we write the measure of the path integral as $D\Omega$ in short that is given in the partition function (5), $A = 1, \dots, N_c$ and $\alpha = 1, \dots, 4$ represent the color and the Dirac indices, respectively and Tr taken for the both indices. The quark propagator is approximated as a sum of contributions from the free and the zero-mode propagators by inverting the Dirac operator in the basis spanned by the quark zero-mode wave functions in instantons background as following [32]

$$\begin{aligned} S(x, y; m) &\approx S_0(x, y) + S^{\text{ZM}}(x, y; m), \\ S_0(x, y) &= \frac{i}{2\pi^2} \frac{\gamma \cdot (x - y)}{(x - y)^4}, \\ S^{\text{ZM}}(x, y; m) &= \sum_{I, J} \left[\psi_{0, I}(x) [(-iT + m)^{-1}]_{IJ} \psi_{0, J}^\dagger(y) \right], \end{aligned} \quad (23)$$

where the matrix T is the overlap matrix given in Eq. (13). Here we omit to write the collective coordinates of instantons $\{U, \rho, z\}$ from the argument of the quark zero-mode wave functions. We obtain the quark condensate by averaging it over the configurations.

D. Monte Carlo simulation

The simplest way to simulate the instanton liquid model described by the Euclid partition function (5) is to use the Monte Carlo method with a weight function S_{eff} given by

$$S_{\text{eff}} = - \sum_{i=1}^{N_+ + N_-} \ln[f(\rho_i)] + S_{\text{int}} - \sum_{f=1}^{N_f} \ln \text{Det}(\not{D} + m_f). \quad (24)$$

To perform Monte Carlo simulations using the Markov Chain Monte Carlo (MCMC) method, it is crucial to understand the weight function S_{eff} . This function represents the probability density $p(\Omega_i)$ as $p(\Omega_i) \propto \exp[-S_{\text{eff}}(\Omega_i)]$, where Ω_i denotes a configuration within the considered ensemble. Once the partition function is established, we derive the weight function, as illustrated in Eq. (24). Employing algorithms such as the Metropolis algorithm or Hybrid Monte Carlo (HMC) algorithm, we generate a series of configurations $\{\Omega\} =$

$(\Omega_1, \Omega_2, \dots, \Omega_{N_{\text{conf}}})$ that converge to the given probability density function because of the detailed balance condition of the algorithms. Here, N_{conf} represents the number of configurations.

The expectation value $\langle O \rangle$ of an operator O that is expressed as a function of a configuration Ω_i is computed from these configurations using the formula:

$$\langle O \rangle = \lim_{N_{\text{conf}} \rightarrow \infty} \frac{1}{N_{\text{conf}}} \sum_{i=1}^{N_{\text{conf}}} O(\Omega_i). \quad (25)$$

For more details on the Monte Carlo simulations using the MCMC, we referred to some textbooks and an introductory article [36–38].

IV. RESULTS

In this section, we will show our numerical results. In subsection IV A, we explain the computational setup and numerical method used for our calculations. In subsection IV B, we show our results of the free energy as a function of the instanton density. In subsection IV C, we present the results of the quark condensate as a function of the instanton density. Combining these results, in subsection IV D, we obtain the free energies as a function of the quark condensate and analyze them near the origin.

A. Computational setup

In our simulations, each configuration Ω_i consists of N_+ instantons and N_- anti-instantons labeled by their collective coordinate $\{U, \rho, z\}$ and the partition function for each instanton density is determined by generating 5000 configurations after 1000 initial sweeps with $N = N_+ + N_- = 16 + 16$ instantons and anti-instantons. The simulations with different instanton density $n = N/V$ are achieved by changing the simulation box size $V = L^4$ with the fixed number of instantons N . Whole simulations are performed under the periodic boundary condition for the coordinates of instantons and anti-instantons. All quantities in this calculation are nondimensionalized by Λ which has been introduced through the β -functions (8). The value of the scale parameter Λ is determined so that the free energy has a minimum value at the instanton density $n = 1 \text{ fm}^{-4}$ [33]. This density with the minimum free energy is the vacuum instanton density. We are interested in the quark condensate dependence of the free energy in the small quark mass regime, so we set the current quark masses m to be as small as possible within a stable run of the simulations. The calculations below are performed with the current quark masses $m = 0.1\Lambda, 0.15\Lambda, 0.2\Lambda$.

In Table I, we show the bulk parameters, such as the current quark mass m , the instanton density in the vacuum n , the scale parameter Λ and the instanton average size $\bar{\rho}$ in our simulations. These values are consistent

TABLE I. The bulk parameters at the vacuum instanton density. The values of the current quark mass m , the vacuum instanton density n , the scale parameter Λ and the instanton average size $\bar{\rho}$ are given. All quantities are given in both the physical unit and Λ . The numbers in square brackets represent the unit of Λ . The superscript * represents the input parameter.

m (MeV)	37.3 [0.1*]	54.1 [0.15*]	70.2 [0.2*]
n (fm^{-4})	1.00* [0.079]	1.00* [0.090]	1.00* [0.10]
Λ (MeV)	373 [1]	360 [1]	351 [1]
$\bar{\rho}$ (fm)	0.35 [0.66]	0.36 [0.66]	0.37 [0.66]

with the previous work [33]. By fixing the unit such that $n = 1 \text{ fm}^{-4}$ at the vacuum, the values of the scale parameter are determined as $\Lambda = 373, 360, 351 \text{ MeV}$ for each current quark mass. Using these values, the average instanton sizes in our calculations are evaluated as $\bar{\rho} = 0.35$ to 0.37 fm compared to $\bar{\rho} = 0.42 \text{ fm}$ in Ref. [33].

To calculate the free energy by Eq. (15), we need the value of the partition function. The partition function is obtained through Eq. (17), so we first calculate Z_0 with the variational single instanton distribution (21). The single instanton distribution can be evaluated from initial 1000 sweeps with full interaction $\alpha = 1$. We calculate the average size squared of instantons $\bar{\rho}^2$ appearing in Eq. (21) using the initial sweeps. The ρ -integral over an infinite interval $[0, \infty]$ appearing in Eq. (21) is practically performed over a finite interval $[0, \Lambda^{-1}]$. The remaining task for the calculation of the partition function is to perform the integral by summing the integrands. This integral is done at 10 different coupling values α .

In the computation of the quark condensate, only the quark zero-mode propagator $S^{\text{ZM}}(x, y; m)$ in Eq. (23) is evaluated to subtract the infinite contribution initiated by the free propagator $S_0(x, x)$ at the same space-time coordinate. In the actual calculations, for each instanton density, the trace of the quark zero-mode propagator is averaged over the 5000 configurations, and also averaged over 10,000 different space-time coordinates to reduce the effect of incomplete equilibration of the configurations.

B. Free energy

In Fig. 2, we show our numerical results of the free energies (in the unit of MeV/fm^3) versus the instanton density (in the unit of fm^{-4}) for three values of the current quark mass. Our results are consistent with the previous work [33]. The free energy is monotonically decreasing towards a minimum value and then rapidly increasing at higher instanton density. This shows that attractive interaction is dominant in lower instanton density regions, while repulsive interaction becomes important at higher instanton density.

In Table II, we summarize our numerical results of the free energy and the quark condensate at the vac-

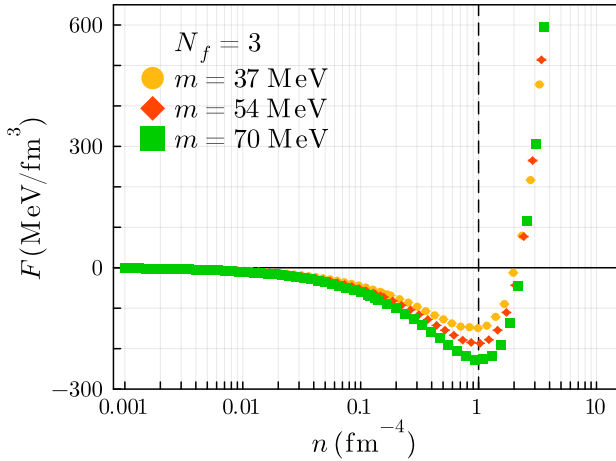


FIG. 2. The free energies as a function of the instanton density for different current quark masses.

TABLE II. The free energy and the quark condensate at the vacuum instanton density with different current quark masses. The notation is the same as in Table I.

$m(\text{MeV})$	37 [0.1*]	54 [0.15*]	70 [0.2*]
$F(\text{MeV}/\text{fm}^3)$	-149[-0.060]	-187[-0.085]	-228[-0.116]
$-\langle\bar{q}q\rangle^{1/3}(\text{MeV})$	-188[-0.12]	-196[-0.16]	-200[-0.18]

uum for three different current quark masses $m = 37, 54, 70$ MeV. By using the values of the scale parameter in Table I, the free energies are evaluated as $F = -149, -187, -228$ MeV/fm³. For reference, we perform further calculations for the current quark masses with values close to those in the previous work, such as $m = 96$ MeV [33]. That shows a good agreement with the previous work, and we conclude that our simulations work well.

C. Quark condensate

In Fig. 3, we show the instanton density dependence of cubic root of the quark condensate $(-\langle\bar{q}q\rangle)^{1/3}$ in the unit of MeV. We find that the absolute values of the quark condensate increase monotonically as the instanton density increases. We also find that the value of the quark condensates at the vacuum is insensitive to the value of the current quark masses. This means that the contribution from the explicit breaking of chiral symmetry due to the current quark mass is not so large for the value of the quark condensate.

In Table II, we show the values of the quark condensate at the vacuum instanton density. Our results almost reproduce the empirical values obtained by various previous works [40–54]. We obtain the values of the quark condensate as $|\langle\bar{q}q\rangle|^{1/3} = 188, 196, 200$ MeV at the vacuum with the current quark masses $m = 37, 54, 70$ MeV,

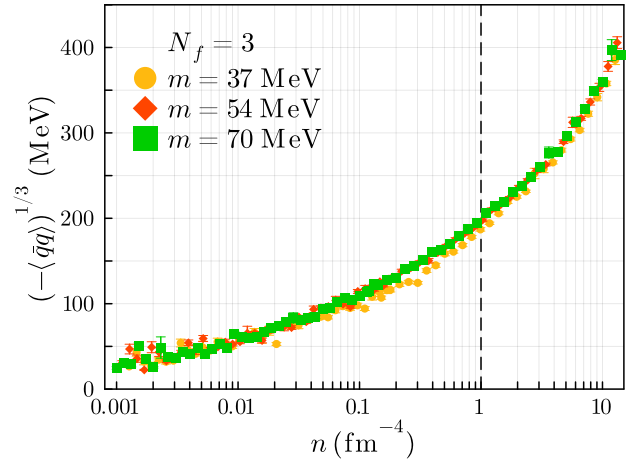


FIG. 3. The quark condensates as a function of the instanton density. Details about the different quark masses are explained in the main text.

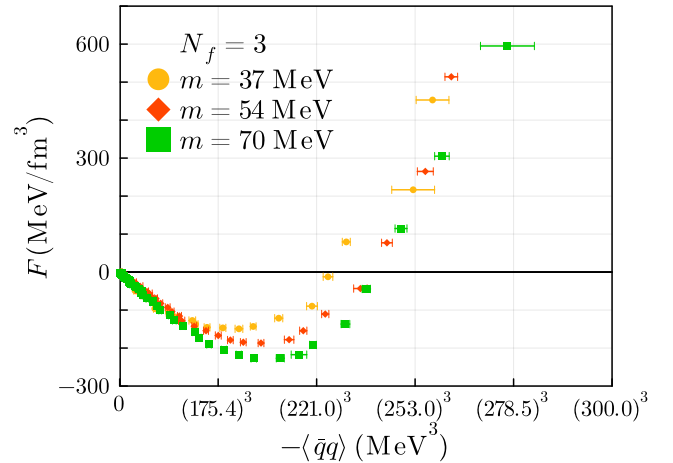


FIG. 4. The free energy densities as a function of the quark condensate for three quark masses. The free energy and the quark condensate are given in the unit of MeV/fm³ and MeV³, respectively.

respectively. These values give a good estimate of the quark condensates although they are slightly smaller in the absolute value.

D. Free energy vs. quark condensate

Combining the results of the free energy and the quark condensate, we obtain the quark condensate dependence of the free energy as shown in Fig. 4. The free energies monotonically decrease towards the minimum values as the quark condensate increases in magnitude. Once the free energies have the minimum value, they start to increase as expected from the instanton density dependence of them (also see Fig. 2). From this, we observe that the

free energy has its minimum value at the point with the finite value of the quark condensate. This shows that chiral symmetry is dynamically broken in the vacuum of the IILM.

The behavior of the free energy near the origin appears to be decreasing in a downward convex trend. This trend is crucial for the sign of the curvature of the free energy at the origin. In other words, it provides one of the hints for discriminating patterns of chiral symmetry breaking through our definition of the determination procedure for the anomaly-driven breaking discussed in Sect. II B. So we study the quark condensate dependence of the free energy more quantitatively.

We aim to evaluate the curvature of the free energy at the origin from our simulation results of the IILM. For that, we perform polynomial fits for our three data sets with different current quark masses. Each data set consists of N_{data} pairs of $\langle \bar{q}q \rangle$ and F , i.e., $(|\langle \bar{q}q \rangle|_i, F_i)$, $i = 1, \dots, N_{\text{data}}$ arranged in ascending order, where N_{data} is the number of data of the free energy and the quark condensate and it is equal to the number of the grid points of the instanton density, $N_{\text{data}} = 71$ in our calculations.

We use a polynomial function given by

$$F(\langle \bar{q}q \rangle) = \sum_{j=0}^K C_j \langle \bar{q}q \rangle^j, \quad (26)$$

for the fitting model in this analysis. We perform the fits for four orders $K = 1, \dots, 4$. For each order K , we optimize the parameters $\{C_j\}$ ($j = 0, \dots, K$) so that they minimize the reduced chi-square including errors of both axes as given in Ref. [55] by

$$\chi_{\text{d.o.f.}}^2 = \frac{1}{N_{\text{d.o.f.}}} \sum_{i=1}^M \frac{(y_i - f(x_i))^2}{\sigma_{y_i}^2 + \sigma_{x_i}^2 [f'(x_i)]^2}, \quad (27)$$

where (x_i, y_i) with their errors $(\sigma_{x_i}, \sigma_{y_i})$ correspond to our data set $(|\langle \bar{q}q \rangle|_i, F_i)$ with their errors, $f(x)$ and $f'(x)$ represent the fit model (26) and its first derivative, $N_{\text{d.o.f.}}$ is the number of degrees of freedom which is defined by $N_{\text{d.o.f.}} \equiv M - (K + 1)$, and M is the number of data used in the fit. We use the data from $i = 1$ to $i = M$ rather all data because we want to know the behavior of the free energy around the origin.

We determine an upper limit of fit range, M , as follows. We calculate the reduced chi-square (27) as we increase the number of data that we use and obtain the reduced chi-square as a function of the number of data. We then find the number of data for which the reduced chi-square has a local minimum value. We finally use this number of data as the value of M for fitting. Here we skip a trivial local minimum obtained with a small number of data. The specific values of M used in each fit, the corresponding quark condensate values and the reduced chi-square are summarized in Table III.

In Table IV, we show the fit results of C_0 . We find that the value of the coefficient C_0 is close to zero. For different fit orders and quark masses, the values of C_0 range

TABLE III. Values of M , the cubic root of the absolute value of the quark condensate in the unit of MeV and the reduced chi-square for each fit with the current quark mass m . The values of current quark mass are given in the unit of MeV.

m	37	54	70
K	$(M, \langle \bar{q}q \rangle ^{1/3}, \chi_{\text{d.o.f.}}^2)$		
1	(41, 125, 3.87)	(25, 79, 3.84)	(40, 131, 4.22)
2	(39, 123, 3.88)	(48, 189, 3.61)	(48, 187, 3.48)
3	(47, 178, 4.01)	(56, 263, 3.16)	(58, 278, 3.06)
4	(48, 187, 4.01)	(62, 353, 3.05)	(58, 278, 3.11)

TABLE IV. Fit results of C_0 for each order K and current quark mass m . Current quark mass m is given in the unit of MeV and the coefficient C_0 is given in the unit of MeV/fm³.

m	37	54	70
K	$C_0(\text{MeV/fm}^3)$		
1	$-0.64_{-0.07}^{+0.07}$	$-1.47_{-0.04}^{+0.04}$	$-1.51_{-0.06}^{+0.06}$
2	$-0.51_{-0.08}^{+0.08}$	$-1.48_{-0.04}^{+0.04}$	$-1.44_{-0.06}^{+0.06}$
3	$-0.47_{-0.08}^{+0.08}$	$-1.51_{-0.04}^{+0.04}$	$-1.48_{-0.06}^{+0.06}$
4	$-0.52_{-0.07}^{+0.07}$	$-1.52_{-0.04}^{+0.04}$	$-1.47_{-0.06}^{+0.06}$

from -1.52 to -0.47 in the unit of MeV/fm³. These values are sufficiently small compared to the typical value of the free energy F and we conclude that the coefficient C_0 is consistent with zero.

In Table V, we show the fit results of C_1 . We find that the value of C_1 is insensitive to the fitting order K . This implies that the value of C_1 is well determined around the origin. We find also that C_1 has no clear quark mass dependence. The averaged values of C_1 over the different orders are 389 MeV, 320 MeV and 360 MeV for $m = 37, 54$ and 70 MeV.

In Table VI, we show the fit results of C_2 . We find that the coefficients C_2 appear to be positive. For each quark mass, the averaged values of C_2 over the different fit orders are $C_2 = (2.94, 0.98, 1.17) \times 10^{-5}$ MeV⁻² for $m = 37, 54$ and 70 MeV. These values of C_2 are located at the positive region for all orders and current quark masses. This suggests that the curvature of the free energy at the origin is positive for the IILM.

In Fig. 5, we show the current quark mass dependence of the coefficient C_2 . The value of C_2 is not very sensi-

TABLE V. Fit results of C_1 for each order K and current quark mass m . The coefficient C_1 is given in the unit of MeV.

m	37	54	70
K	$C_1(\text{MeV})$		
1	$364.0_{-5.6}^{+5.6}$	$332.5_{-9.7}^{+9.1}$	$349.3_{-4.6}^{+4.5}$
2	$395.8_{-6.0}^{+5.7}$	$326.2_{-1.4}^{+1.4}$	$371.8_{-1.8}^{+1.7}$
3	$403.9_{-0.6}^{+0.6}$	$312.6_{-0.4}^{+0.4}$	$358.1_{-0.7}^{+0.7}$
4	$391.9_{-0.6}^{+0.6}$	$307.9_{-0.4}^{+0.6}$	$361.8_{-0.7}^{+0.7}$

TABLE VI. Fit results of C_2 for each order K and current quark mass m . The coefficient C_2 is given in the unit of MeV^{-2} .

m	37	54	70
K	$C_2 \times 10^5 (\text{MeV}^{-2})$		
1	-	-	-
2	$3.46^{+0.52}_{-0.58}$	$1.71^{+0.03}_{-0.03}$	$1.74^{+0.03}_{-0.04}$
3	$3.51^{+0.01}_{-0.01}$	$0.78^{+0.01}_{-0.01}$	$0.79^{+0.01}_{-0.01}$
4	$1.84^{+0.01}_{-0.01}$	$0.44^{+0.01}_{-0.01}$	$0.99^{+0.01}_{-0.01}$

TABLE VII. Fit results of C_2 in the quenched calculations for each order K and current quark mass m . The coefficient C_2 is given in the unit of MeV^{-2} .

Quenched			
m	2.8	14	28
K	$C_2 \times 10^5 (\text{MeV}^{-2})$		
1	-	-	-
2	$-3.97^{+0.08}_{-0.08}$	$-3.48^{+0.11}_{-0.11}$	$-2.40^{+0.11}_{-0.11}$
3	$-3.32^{+0.10}_{-0.10}$	$-4.39^{+0.07}_{-0.07}$	$-3.22^{+0.08}_{-0.08}$
4	$-2.72^{+0.26}_{-0.23}$	$-3.61^{+0.01}_{-0.01}$	$-2.11^{+0.01}_{-0.01}$

tive to the value of the current quark mass. For the fit with the smallest quark mass, the values of C_2 are evaluated as slightly larger than the results of other two quark masses. These results suggest that the value of C_2 and the curvature of the free energy at the origin is positive for wide current quark mass region and thus we conclude that the anomaly-driven breaking of chiral symmetry is realized in the IILM by our definition (4)

Here we do not show the values of the coefficients C_3 and C_4 because these coefficients are introduced to confirm the stability of fits of C_0 , C_1 and C_2 with and without these higher-order terms. Furthermore, since we use the part of full data near the origin for fits, the values of C_3 and C_4 are not determined well and irrelevant to our discussion.

Interestingly we find the opposite sign of C_2 in the quenched calculations where the quark determinant part in the partition function (5) is set as $\prod_f \text{Det}(\not{D} + m_f) = 1$ in generating the configurations. The details of the quenched calculation are shown in Appendix A. As we show in Table VII, the quenched calculations suggest the negative values of coefficient C_2 . By our definition of the anomaly-driven breaking (4), this concludes that the normal breaking is realized in the quenched IILM. The opposite signs of C_2 obtained by the full and quenched calculations mean that the different scenarios of chiral symmetry breaking are possible depending on the presence of the quark determinant part in the IILM partition function. Since the quark determinant contributes to the instanton-quark interaction in the ensemble, this implies that the quarks play a crucial role in the anomaly-driven breaking for the IILM.

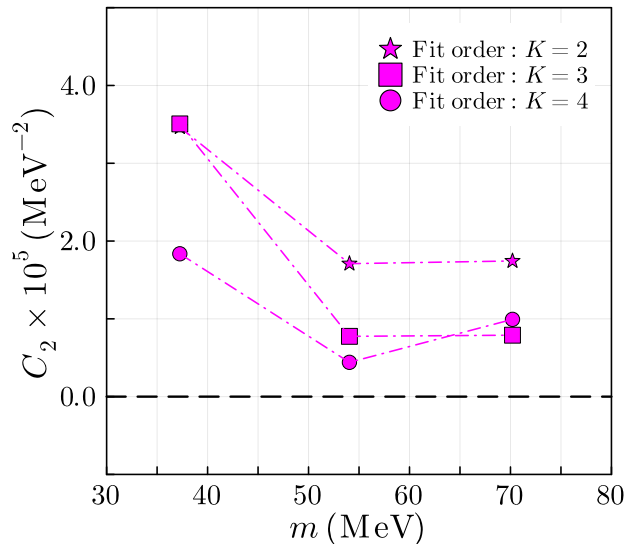


FIG. 5. Current quark mass dependence of the coefficient C_2 . Fit results of different orders are shown with different types of markers. Error bars are omitted because they are small.

V. CONCLUSIONS

We have examined the possibility of the chiral symmetry breaking scenario that can be realized when the $U(1)_A$ anomaly contribution is sufficiently large using the IILM. Following the NJL model, we have generalized the determination procedure for the pattern of chiral symmetry breaking. We use the second-order differential coefficient of the vacuum energy density with respect to the quark condensate at the origin, e.g., the curvature. We have defined that the pattern of chiral symmetry breaking is the normal or the anomaly-driven one if the curvature is negative or positive, respectively.

We have found that the curvature appears to be positive in the IILM. This means that the anomaly-driven breaking is feasible in the IILM by our definition. In contrast to that, the quenched calculations show the negative curvature and support the realization of the normal chiral symmetry breaking in the quenched IILM. These results indicate that the instanton-quark interaction is crucial to realize the anomaly-driven breaking because the difference between the full and quenched IILM is the presence or absence of the quark determinant that contributes to the interaction among instantons and the dynamical quarks.

One important direction for future development is to investigate the mass of mesons, such as σ and η' . As discussed in the previous work [28], chiral effective theories concluded that the σ mass could be smaller than 800 MeV in the anomaly-driven symmetry breaking. We expect the same conclusions to be drawn in the IILM. Even if such conclusions cannot be reached, it is interesting to clarify the differences between the chiral effective

TABLE VIII. The bulk parameters at the vacuum instanton density for the quenched calculation. The asterisk represents the value of the input fix parameter.

Quenched	
n (fm $^{-4}$)	1.00* [0.24]
Λ (MeV)	281 [1]
$\bar{\rho}$ (fm)	0.42 [0.60]
F (MeV/fm 3)	-532 [-0.657]

theories and the IILM. Computation with different flavors, e.g., $N_f = 2$, using the IILM may provide further insights into the anomaly-driven breaking in QCD. These are subjects to be investigated in future studies.

ACKNOWLEDGMENTS

We would like to thank Masayasu Harada for useful discussions and comments. We also thank Masakiyo Kitazawa and Kotaro Murakami for their advice. This work of Y.S. was partly supported by the Advanced Research Center for Quantum Physics and Nanoscience, Tokyo Institute of Technology, and JST SPRING, Grant Number JPMJSP2106. The work of D.J. was supported in part by Grants-in-Aid for Scientific Research from JSPS (JP21K03530, JP22H04917 and JP23K03427).

Appendix A: Results of the quenched calculations

We show the numerical results for the quenched calculations. The quenched calculations can be performed in the same way as in the full calculations except for setting the quark determinant in the partition function to unity. The following numerical results of the quenched calculations are obtained by the same setup as the full calculations, that is, 5000 configurations after 1000 initial sweeps with $N = N_+ + N_- = 16 + 16$ instantons and anti-instantons. In the quenched calculations, the current quark mass enters only the calculation of the quark condensate through the quark zero-mode propagator (23).

In Table VIII, we show the bulk parameters of the quenched ensemble. These values are consistent with the quenched calculation in the previous work [33]. We obtain the scale parameter $\Lambda = 281$ MeV and the average instanton size $\bar{\rho} = 0.42$, which are compared to $\Lambda = 270$ MeV and $\bar{\rho} = 0.43$ fm in the previous work [33], respectively. Our result of the free energy $F = -532$ MeV/fm 3 shows a good agreement with $F = -526$ MeV/fm 3 for the quenched calculation in Ref. [33]. Our result also shows a good agreement with the estimation from the trace anomaly $F = -543$ MeV/fm 4 as discussed in Ref. [33].

In Table IX, we show the quark condensate at the vacuum for three current quark masses. Our results of the

TABLE IX. The quark condensates at the vacuum for the quenched calculations with different quark masses. The asterisk represents the value of the input fix parameter.

m (MeV)	2.8 [0.01*]	14 [0.05*]	28 [0.1*]
$-\langle\bar{q}q\rangle^{1/3}$ (MeV)	-246 [-0.67]	-244 [-0.65]	-233 [-0.57]

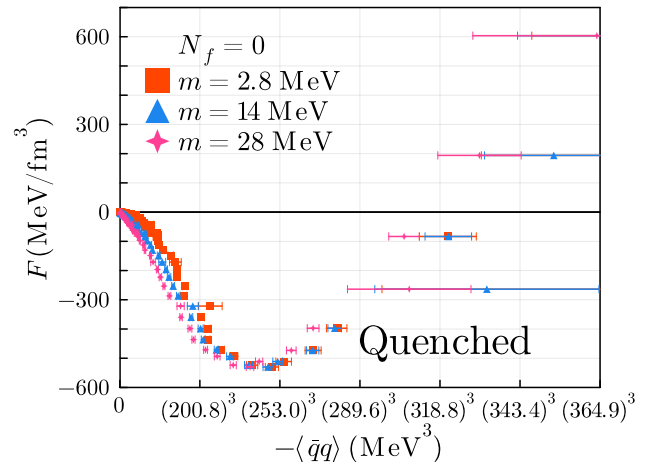


FIG. 6. The free energies as a function of the quark condensate in the quenched calculations.

quark condensate $|\langle\bar{q}q\rangle|^{1/3} = 246, 244, 233$ MeV for the current quark masses $m = 2.8, 14, 28$ MeV almost reproduce the empirical values obtained by various previous works [40–54]. We conclude that our simulations also work well in the quenched calculations.

In Fig. 6, we show the free energy versus the quark condensate for the quenched calculations. This shows globally almost same behavior with the results of the unquenched calculations, but the trend of the free energy near the origin appears to be slightly different from the unquenched results. We perform the same analysis to the unquenched calculations using the polynomial fitting and show the fit results following.

In Table X, we show the fit results of C_0 for the quenched calculations. We find that the value of the

TABLE X. Fit results of C_0 in the quenched calculations for each order K and current quark mass m . Current quark mass m is given in the unit of MeV and the coefficient C_0 is given in the unit of MeV/fm 3 .

Quenched			
m	2.81	14.04	28.08
K	C_0 (MeV/fm 3)		
1	$-0.47^{+0.04}_{-0.04}$	$-0.72^{+0.03}_{-0.03}$	$-0.76^{+0.02}_{-0.02}$
2	$-0.74^{+0.03}_{-0.03}$	$-0.76^{+0.02}_{-0.02}$	$-0.80^{+0.02}_{-0.02}$
3	$-0.70^{+0.03}_{-0.03}$	$-0.78^{+0.02}_{-0.02}$	$-0.81^{+0.02}_{-0.02}$
4	$-0.69^{+0.03}_{-0.03}$	$-0.76^{+0.02}_{-0.02}$	$-0.80^{+0.02}_{-0.02}$

TABLE XI. Fit results of C_1 in the quenched calculations for each order K and current quark mass m . The coefficient C_1 is given in the unit of MeV.

Quenched			
m	2.81	14.04	28.08
K	$C_1(\text{MeV})$		
1	$64.1^{+2.1}_{-2.2}$	$180.9^{+3.6}_{-3.8}$	$329.6^{+3.9}_{-3.9}$
2	$38.6^{+1.5}_{-1.7}$	$168.3^{+2.5}_{-2.7}$	$308.1^{+3.1}_{-3.1}$
3	$41.9^{+1.7}_{-1.7}$	$162.1^{+2.4}_{-2.4}$	$302.3^{+2.8}_{-2.8}$
4	$43.8^{+1.4}_{-1.4}$	$166.3^{+1.4}_{-1.4}$	$308.4^{+1.0}_{-0.8}$

coefficient C_0 is also close to zero. The value of C_0 averaged over different orders and quark masses is $C_0 = -0.77 \text{ MeV/fm}^3$. This value is sufficiently small compared to the typical value of the free energy F and we conclude that the coefficient C_0 is also consistent with

zero in the quenched calculation.

In Table XI, we show the fit results of C_1 for the quenched calculations. We find that the coefficient C_1 increases monotonically as the current quark mass increases. For each quark mass, we average the values of C_1 over the different orders and obtain $C_1 = 48 \text{ MeV}$, 169 MeV and 312 MeV for $m = 2.8, 14$ and 28 MeV , respectively. We conclude that the value of C_1 increases monotonically as the quark mass increases for the quenched calculations.

In Fig. 7, we show the current quark mass dependence of the coefficient C_2 for the quenched calculations. For all quark masses, the value of C_2 appears to be negative in different fit orders. As we have discussed in Sect. IV D, these results suggest that the chiral symmetry is broken in the normal way for the quenched ILM by our definition (4).

- [1] J. R. Peláez, “From controversy to precision on the sigma meson: A review on the status of the non-ordinary $f_0(500)$ resonance,” Phys. Rept. **658** (2016) 1.
- [2] R. L. Workman, *et al.*, (Particle Data Group), “Review of Particle Physics,” Prog. Theor. Exp. Phys. **2022**, 083C01 (2022).
- [3] R. J. Jaffe, “Multiquark hadrons. I. Phenomenology of $Q^2\bar{Q}^2$ mesons,” Phys. Rev. D **15** (1977) 267.
- [4] J. A. Oller, E. Oset, “Meson-meson interactions in a non-perturbative chiral approach,” Phys. Rev. D **59** (1999) 074001; Erratum: [Phys. Rev. D **60** (1999) 099906, Phys. Rev. D **75** (2007) 099903].
- [5] D. Black, A. H. Fariborz, F. Sannino, J. Schechter, “Putative light scalar nonet,” Phys. Rev. D **59** (1999) 074026.
- [6] M. Ishida, “Possible Classification of the Chiral Scalar σ -Nonet,” Prog. Theor. Phys. **101** (1999) 661.
- [7] G. Colangelo, J. Gasser, H. Leutwyler, “ $\pi\pi$ scattering,” Nucl. Phys. B **603** (2001) 125.
- [8] T. Kunihiro, S. Muroya, A. Nakamura, C. Nonaka, M. Sekiguchi, H. Wada, “Scalar mesons in lattice QCD,” Phys. Rev. D **70** (2004) 034504.
- [9] M. Napsuciale, S. Rodriguez, “Chiral model for $\bar{q}q$ and $\bar{q}qqq$ mesons,” Phys. Rev. D **70** (2004) 094043.
- [10] J. R. Peláez, “Light scalars as tetraquarks or two-meson states from large- N_c and unitarized chiral perturbation theory,” Mod. Phys. Lett. A **39** (2004) 2879.
- [11] I. Caprini, G. Colangelo, H. Leutwyler, “Mass and Width of the Lowest Resonance in QCD,” Phys. Rev. Lett. **96** (2006) 132001.
- [12] M. R. Pennington, “Location, correlation, radiation: Where is the σ , what is its structure, and what is its coupling to photons?,” Mod. Phys. Lett. A **22** (2007) 1439.
- [13] A. H. Fariborz, R. Jora, J. Schechter, “Global aspects of the scalar meson puzzle,” Phys. Rev. D **79** (2009) 074014.
- [14] T. Hyodo, D. Jido, T. Kunihiro, “Nature of the σ meson as revealed by its softening process,” Nucl. Phys. A **848** (2010) 341.
- [15] G. Mennessier, S. Narison, X.-G. Wang, “ σ and $f_0(980)$

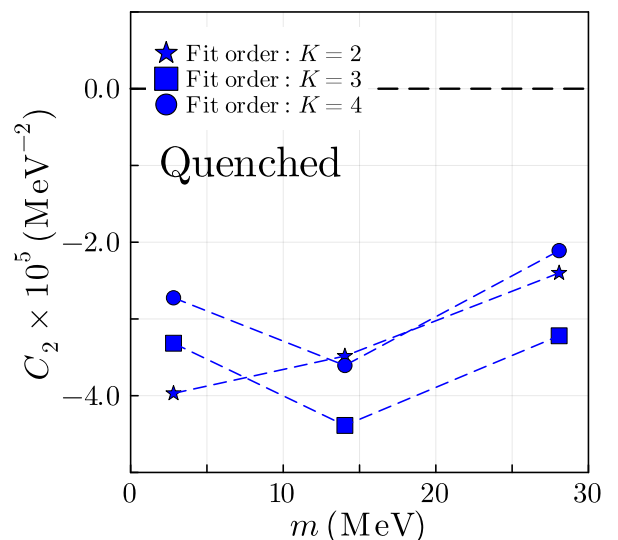


FIG. 7. Current quark mass dependence of the coefficient C_2 for the quenched calculations. Fit results of different orders are shown with different markers. Error bars are omitted because they are small. Values are summarized in Table VII.

- substructures from $\gamma\gamma \rightarrow \pi\pi, J/\psi, \phi$ radiative and D_s semi-leptonic decays,” Phys. Lett. B **696** (2004) 40.
- [16] D. Parganlija, P. Kovács, Gy. Wolf, F. Giacosa, D. H. Rischke, “Meson vacuum phenomenology in a three-flavor linear sigma model with (axial-)vector mesons,” Phys. Rev. D **87** (2013) 014011.
- [17] J. R. Peláez, A. Rodas, J. Ruiz de Elvira, “Strange resonance poles from $K\pi$ scattering below 1.8 GeV,” Eur. Phys. J. C **77** (2017) 91.
- [18] M. Ablikim, *et al.* (BESIII Collaboration), “Observation of $D^+ \rightarrow f_0(500)e^+\nu_e$ and Improved Measurements of $D \rightarrow \rho e^+\nu_e$,” Phys. Rev. Lett. **122** (2019) 062001.

- [19] N. R. Soni, A. N. Gadaria, J. J. Patel, J. N. Pandya, “Semileptonic decays of charmed mesons to light scalar mesons,” *Phys. Rev. D* **102** (2020) 016013.
- [20] N. N. Achasov, J. V. Bennett, A. V. Kiselev, E. A. Kozyrev, G. N. Shestakov, “Evidence of the four-quark nature of $f_0(980)$ and $f_0(500)$,” *Phys. Rev. D* **103** (2021) 014010.
- [21] J. R. Peláez, A. Rodas, J. Ruiz de Elvira, “Precision dispersive approaches versus unitarized chiral perturbation theory for the lightest scalar resonances $\sigma/f_0(500)$ and $\kappa/K_0^*(700)$,” *Eur. Phys. J. Spec. Top.* **230** (2021) 1539.
- [22] M. Gell-Mann, M. Lévy, “The Axial Vector Current in Bet Decay,” *Nuovo. Cim.* **16** (1960) 705.
- [23] Y. Nambu, G. Jona-Lasinio, “Dynamical Model of Elementary Particles Based on an Analogy with Superconductivity. I,” *Phys. Rev.* **112** (1961) 345.
- [24] J. J. M. Verbaarschot, T. Wettig, “Random matrix theory and chiral symmetry in QCD,” *Ann. Rev. Nucl. Part. Sci.* **50** (2000) 343.
- [25] E. Witten, “Current algebra theorem for the $U(1)$ Goldstone Boson,” *Nucl. Phys. B* **156** (1979) 269.
- [26] G. ’t Hooft, “Symmetry breaking through Bell–Jackiw anomalies,” *Phys. Rev. Lett.* **37** (1976) 8.
- [27] G. ’t Hooft, “Computation of the quantum effects due to four-dimensional pseudoparticle,” *Phys. Rev. D* **14** (1976) 3432.
- [28] S. Kono, D. Jido, Y. Kuroda, and M. Harada, “The role of $U_A(1)$ breaking term in dynamical chiral symmetry breaking of chiral effective theories,” *PTEP* **2021**, no. 9, 093D02 (2021).
- [29] E. V. Shuryak, “The role of instantons in quantum chromodynamics: (I). Physical vacuum,” *Nucl. Phys. B* **203** (1982) 93.
- [30] E. V. Shuryak, “The role of instantons in quantum chromodynamics: (II). Hadronic structure,” *Nucl. Phys. B* **203** (1982) 116.
- [31] G. ’t Hooft, “How Instantons Solve the $U(1)$ Problem,” *Phys. Rept.* **142**, 357 (1986).
- [32] T. Schäfer and E. V. Shuryak, “Instantons in QCD,” *Rev. Mod. Phys.* **70** (1998) 323.
- [33] T. Schäfer and E. V. Shuryak, “Interacting instanton liquid model in QCD at zero and finite temperature,” *Phys. Rev. D* **53** (1996) 6522.
- [34] A. V. Yung, “Instanton vacuum in supersymmetric QCD,” *Nucl. Phys. B* **297** (1988) 47.
- [35] J. J. M. Verbaarschot, “Streamlines and conformal invariance in Yang–Mills theories,” *Nucl. Phys. B* **362** (1991) 33.
- [36] K. Binder and D. Herrmann, “Monte Carlo Simulations in Statistical Physics An Introduction (6th ed.),” Springer Berlin, Heidelberg (2010).
- [37] D. Randau and K. Binder, “A Guide to Monte Carlo Simulations in Statistical Physics,” Cambridge Univ. Press. (2014).
- [38] M. Hanada, “Markov Chain Monte Carlo for Dummies,” arXiv:1808.08490.
- [39] M.A. Shifman, A.I. Vainshtein, V.I. Zakharov, “QCD and resonance physics. Applications,” *Nucl. Phys. B* **147** (1979) 448.
- [40] M. Gell-Mann, R.J. Oakes, B. Renner, “Behavior of current divergences under $SU_3 \times SU_3$,” *Phys. Rev.* **175** (1968) 2195.
- [41] L.J. Reinders, H. Rubinstein, S. Yazaki, “Hadron properties from QCD sum rules,” *Phys. Rep.* **127** (1985) 1.
- [42] H.G. Dosch, S. Narison, “Direct extraction of the chiral quark condensate and bounds on the light quark masses,” *Phys. Lett. B* **417** (1998) 173.
- [43] D. Harnett, J. Ho, T.G. Steele, “Correlations between the strange quark condensate, strange quark mass, and kaon PCAC relation,” *Phys. Rev. D* **103** (2021) 114005.
- [44] L. Giusti, C. Hoelbling, C. Rebbi, “Light quark masses with overlap fermions in quenched QCD,” *Phys. Rev. D* **64** (2001) 114508.
- [45] C. McNeile, A. Bazavov, C.T.H. Davies, R.J. Dowdall, K. Hornbostel, G.P. Lepage, H.D. Trottier, “Direct determination of the strange and light quark condensate from full lattice QCD,” *Phys. Rev. D* **87** (2013) 034503.
- [46] S. Borsányi, S. Dürr, Z. Fodor, S. Krieg, A. Schäfer, E.E. Scholz, K.K. Szabó, “ $SU(2)$ chiral perturbation theory low-energy constants from $2+1$ flavor staggered lattice simulations,” *Phys. Rev. D* **88** (2013) 014513.
- [47] S. Dürr, Z. Fodor, C. Hoelbling, S. Krieg, T. Kurth, L. Lellouch, T. Lippert, R. Malak, T. Métivet, A. Portelli, A. Sastre, K.K. Szabó, “Lattice QCD at physical point meets $SU(2)$ chiral perturbation theory,” *Phys. Rev. D* **90** (2014) 114504.
- [48] G. Cossu, H. Fukaya, S. Hashimoto, T. Kaneko, J. Noaki, “Stochastic calculation of the Dirac spectrum on the lattice and a determination of chiral condensate in $2+1$ flavor QCD,” *PTEP* **2016** (2016) 093B06.
- [49] C.T.H. Davies, K. Hornbostel, J. Komijani, J. Koponen, G.P. Lepage, A.T. Lytle, C. McNeile, HPQCD collaboration, “Determination of the quark condensate from heavy-light current-current correlators in full lattice QCD,” *Phys. Rev. D* **100** (2019) 034506.
- [50] FLAG collaborations, “FLAG Review 2021,” *Eur. Phys. J. C* (2022) 82:869.
- [51] J. Gasser, H. Leutwyler, “Chiral perturbation theory: expansions in the mass of the strange quark,” *Nucl. Phys. B* **250** (1985) 465.
- [52] M. Jamin, “Flavour-symmetry breaking of the quark condensate and chiral corrections to the Gell–Mann–Oakes–Renner relation,” *Phys. Lett. B* **538** (2001) 71.
- [53] P.A. Boyle, N.H. Christ, N. Garron, C. Jung, A. Jüttner, C. Kelly, R.D. Mawhinney, G. McGlynn, D.J. Murphy, S. Ohta, A. Portelli, C.T. Sachrajda, “Low energy constants of $SU(2)$ partially quenched chiral perturbation theory from $N_f = 2+1$ domain wall QCD,” *Phys. Rev. D* **93** (2016) 054502.
- [54] J. Kneur, A. Neveu, “Chiral condensate and spectral density at full five-loop and partial six-loop orders of renormalization group optimized perturbation theory,” *Phys. Rev. D* **101** (2020) 074009.
- [55] J. Orear, “Least squares when both variables have uncertainties,” *Am. J. Phys.* **50** (1982) 912, Erratum: [*Am. J. Phys.* **52** (1984) 278].